



Grain refining enables mixed Cu⁺/Cu⁰ states for CO₂ electroreduction to C₂₊ products at high current density

Xiangzhou Lv^a, Qian Liu^a, Jianghao Wang^b, Xiuju Wu^a, Xiaotong Li^a, Yue Yang^a, Jianhua Yan^c, Angjian Wu^{c,*}, Hao Bin Wu^{a,*}

^a Institute for Composites Science Innovation (InCSI) and State Key Laboratory of Silicon Materials, School of Materials Science and Engineering, Zhejiang University, Hangzhou 310027, PR China

^b Institute of Zhejiang University-Qizhou, 78 Jiuhua Boulevard North, Quzhou 324000, PR China

^c State Key Laboratory of Clean Energy Utilization, Zhejiang University, Hangzhou 310027, PR China



ARTICLE INFO

Keywords:

Electrochemical CO₂ reduction
Valence states
Grain boundaries
C₂₊ products
C-C coupling

ABSTRACT

The oxidation status of Cu-based materials have been proved to be essential to the catalytical performances of electrochemical CO₂ reduction. The coexistence of Cu⁺ and Cu⁰ species is generally considered as the origin of superior catalytic performance, yet the Cu⁺ moieties are subject to reduction under negative potentials especially at high current density. In this work, we report a grain refining approach to tune the oxidation states of Cu-based catalysts by modulating the electron transfer during electrochemical CO₂ reduction reaction (CO₂RR) process when the in-situ electroreduction of Cu⁺ species occurs. Cu₂O nanospheres with abundant grain boundaries exhibited lower electron conductivity compared with Cu₂O nanospheres with less grain boundaries, which can hinder the complete reduction of Cu₂O and maintain Cu⁺ species under high current densities. As a result, the multi-grain Cu₂O showed a maximum FE of ~79% for C₂₊ products at a high current density of 800 mA cm⁻², notably surpassing the later. Experimental and theoretical analyses indicated that mixed Cu⁺/Cu⁰ states of multi-grain Cu₂O during reaction, favoring the C-C coupling process towards C₂₊ products. This work demonstrates the feasibility to tune the real valence state of catalytic sites under operational conditions by nanostructure engineering.

1. Introduction

Electrochemical CO₂ reduction is a promising technology to convert CO₂ into multiple value-added products using sustainable solar or wind energy [1–3]. Cu-based electrocatalysts have been proven to produce quantities of multi-carbon hydrocarbons and oxygenated fuels (C₂₊ products) via electrochemical CO₂ reduction reaction [4–7]. While the detailed reaction mechanism of CO₂ reduction reaction (CO₂RR) on Cu-based electrocatalysts has not been elaborated clearly, the oxidation states and chemical valences of Cu have been known to strongly correlate with the catalytic performance [8–13]. Particularly, oxide-derived Cu catalysts have been reported to show improved activity and selectivity towards C₂ products (ethylene and ethanol) compared with pristine Cu foil electrode [11,14–16]. It has been generally accepted that the presence of Cu⁺ species during CO₂RR process is the main reason for this superior catalytic performance [16,17]. Further experimental evidences indicated that the mixture of Cu⁺ and Cu⁰ enhances multi-carbon

production (especially C₂H₄) from CO₂ reduction [10–12,18,19]. Such observation has been supported by recent quantum mechanics calculation, which revealed that the synergy between surface Cu⁺ and Cu⁰, rather than single-valence sites, significantly promoted both CO₂ activation and CO dimerization, favoring the production of C₂₊ products [20].

However, copper oxides would be easily reduced to metallic Cu⁰ under CO₂RR condition, and regulating the oxidation state of Cu catalysts during electrolysis reminds a big challenge [21–24]. Heteroatom doping [12,18,25], alloying [26] and surface modification [9] have been demonstrated to create or preserve the Cu⁺ moieties thus promoting the generation of C₂₊ products. However, these strategies usually require precise control over the chemical compositions. Pulse electroreduction that can in-situ produce Cu₂O has also been reported to regulate the oxidation state of Cu foil during CO₂RR process [27], yet the mechanistic exploration and implementation in practical devices remain difficult due to the complicated reaction environment [28]. While

* Corresponding authors.

E-mail addresses: wuaj@zju.edu.cn (A. Wu), hbwu@zju.edu.cn (H.B. Wu).

reaction intermediates have been reported to stabilize surface oxide/hydroxide species on Cu foil [29], modulating the adsorption of intermediates demands precise design on the nanostructures of electrocatalysts [30]. Overall, existing methods to preserve the Cu⁺ species during CO₂RR are rather circumscribed, which limits the capability to tune the valence state of Cu-based catalysts.

Herein, we demonstrate a grain refining approach to tune the valence states of Cu-based catalysts by modulating the electron transfer for the in-situ electroreduction of Cu⁺ species during CO₂RR. As a proof of concept, Cu₂O nanospheres composed of small grains have been shown to maintain a mixed Cu⁺/Cu⁰ states at high current densities during CO₂RR, enabling highly efficient C₂₊ products formation by CO₂RR. The abundant grain boundaries within the Cu₂O nanospheres would inhibit the complete reduction of Cu⁺, and provide numerous defect sites as catalytic active centers. The Cu₂O nanospheres with abundant grain boundaries maintain a high FE of ~79% and a maximum partial current density of around 700 mA cm⁻² for C₂₊ products, in contrast to the Cu₂O nanospheres with few grain boundaries producing large quantity of H₂/CH₄ under similar condition. The origins of the remarkable catalytic activity have been explicitly explored by both experimental and theoretical analysis, providing some design guidelines for valence modulation of electrocatalysts.

2. Experimental section

2.1. Materials and methods

2.1.1. Materials

CuSO₄·5H₂O (> 99.0%), Cu(OAc)₂·H₂O (> 98.0%), NaOH (> 96.0%), L-Ascorbic acid (> 99.7%), N₂H₄·xH₂O (> 85.0%) were purchased from Sinopharm Chemical Reagent Co., KOH (> 95%) was purchased from Macklin Biochemical Co., Ltd. Multi-walled carbon nanotubes (MWCNTs) were purchased from Xianfeng Nano Co., Ltd. (Nanjing, China) and carbon black (CB) was purchased from Cabot Corporation. All chemical reagents were of analytical grade and used without further purification.

2.1.2. Synthesis of Cu₂O-1

1 mmol Cu(OAc)₂·H₂O was dissolved in 40 ml deionized water to form transparent solution, then 200 μl 85% N₂H₄ was slowly dropped into the solution under stable magnetic stirring for 25 mins. The mixture was centrifuged to collect the solid powder and washed with deionized water for twice and ethanol for once before drying in a vacuum oven at 60 °C overnight.

2.1.3. Synthesis of Cu₂O-2

2 mmol CuSO₄·5H₂O was added into 40 ml 0.1 M NaOH solution under magnetic stirring. After that, 2 mmol L-Ascorbic acid was added into the blue mixture and kept magnetic stirring for 30 mins. The final mixture was centrifuged and the collected powder was washed with deionized water for twice followed by ethanol for once before drying in a vacuum oven at 60 °C overnight.

2.2. Characterizations

The morphologies of two kinds of Cu₂O and their corresponding electrodes after electrochemical CO₂ reduction (AECR) were studied using scanning electron microscopy (SEM) on a Phenom LE microscope equipped with an Energy Disperse Spectroscopy (EDS). TEM images of two kinds of Cu₂O before and after CO₂RR was obtained using Jeol JEM-2100 F at the voltage at 200 KV. All the X-ray diffraction (XRD) patterns were obtained using Panalytical X'Pert3 X-ray Powder Diffractometer with Cu K α X-rays. X-ray photoelectron spectroscopy (XPS) was performed using a Thermo Scientific K-Alpha spectrometer using mono Al K α source. UV-Vis spectra were recorded on SHIMADZU UV3600 ultraviolet and visible spectrophotometer under diffuse reflection mode.

The Brunauer–Emmett–Teller (BET) specific surface areas of samples were measured on a physical adsorption instrument Micromeritics ASAP2460. The Temperature Programmed Desorption (TPD) was conducted with AutoChem1 II 2920. Grain sizes of the Cu₂O nanospheres were determined by the Scherrer equation: $D=K\lambda/(\beta\cos\theta)$; where D is the grain size that corresponding to the Cu₂O (111) direction; K value is usually equal to 1; λ is the wavelength of the X-ray; β is the half-height width of the specific diffraction peak and θ is the diffraction angle.

2.3. Electrochemical evaluation

2.3.1. Electrodes preparation

To prepare the gas diffusion electrodes (GDEs) used in the flow cell, 15 mg catalyst was mixed with 60 μl 5 wt% Nafion dispersion in 1.5 ml DI water and 2 ml ethanol. The mixture was ultrasonically dispersed for 30 mins to form homogeneous ink and 2 ml ink was air-brushed onto the hydrophobic gas diffusion layer (2.5 cm * 2.5 cm). The catalysts loading was estimated to be ~0.4 mg cm⁻² by weighing the GDE before and after catalysts deposition. To evaluate the redox behavior of different Cu₂O, the catalysts were directly deposited onto the glassy carbon (GC) electrodes. For the electrode preparation, 5 mg of catalyst was mixed with 20 μl 5 wt% Nafion dispersion in 250 μl DI water and 250 μl ethanol. After ultrasonic to form homogeneous ink, 10 μl of the ink was pipetted onto the glassy carbon electrode with a diameter of 5 mm. The electrode was allowed to dry at ambient condition for further characterization. For the Cu₂O-2/CNTs or CB electrodes (both GDE and GC electrodes) with different carbon loading, the preparation process was mostly the same except that a different amount of MWCNTs/CB was added.

2.3.2. Electrochemical CO₂ reduction

CO₂ electrolysis was conducted in 2 M KOH with our homemade three-compartment (gas, cathodic and anodic chambers) flow cell setup. The circular windows for electrolysis were set to be 16 mm for both the cathode and anode, yielding an activity area of 2 cm². The two chambers for catholyte and anolyte were made of polymethyl methacrylate (PMMA), each chamber had an inlet and an outlet for electrolyte to flow via a peristaltic pump. A Hg/HgO reference electrode was fixed in the catholyte chamber near to the cathode GDE to decrease the solution resistance (R_u). The cathode GDEs were placed between the current collector and the electrolyte chamber with the microporus layer (MPL) facing the cathode electrolyte and a piece of Ni foam was used as anode directly facing the anode electrolyte. Silicone gaskets with a 16 mm diameter circular window were placed between GDE and the electrolyte chamber for sealing. An anion exchanged membrane (AEM, Fumasep FAB-PK-130) was used to separate the catholyte and anolyte chambers. All the pieces were pressed together by four pairs of screws and nuts at the four corners. Before CO₂ electrolysis, the electrodes were activated by the CV method and R_u was measured by electrochemical impedance spectroscopy (EIS) analyses after activation using the Bio-Logic VSP potentiostat. CO₂ electrolysis was conducted under different current densities using CHI 760e electrochemical workstation equipped with a current booster under chronopotentiometry mode. The potential converted to versus RHE with iR corrected was obtained by the following equation:

$$E_{RHE} = E_{Hg/HgO} + 0.0592 \cdot pH + 0.098 - iR_u$$

The gas outlet of the cathodic compartment was connected to an online gas chromatograph (GC9790Plus, FULI INSTRUMENTS) for analysis, which equipped with TCD detector to analyze H₂ and FID detector to analyze CO and hydrocarbon products. Liquid products were analyzed via nuclear magnetic resonance spectroscopy (NMR) from respective catholyte solutions. ¹H NMR spectra were collected on Bruker 400 M spectrometer in D₂O in water suppression mode using DMSO as the internal standard.

2.3.3. ECSA measurement

The ECSA of different electrodes was compared using the electric double-layer capacitance (C_{dl}). To measure this, CV scans were recorded at different scan rates in the non-Faradaic potential region. The currents density at a given potential (usually the intermediate value of the non-Faradaic potential region) were recorded from the forward and reverse scans. The difference between these currents densities divided by two was plotted against the scan rate to obtain a straight line. The slope of this line corresponds to the capacitance of the catalyst's electric double-layer capacitance. Measurements were conducted under constant CO_2 flow and recirculation of 2 M KOH electrolyte.

2.3.4. Half-cell energy efficiency

The calculation of the half-cell energy efficiency (EE) towards C_{2+} products of the two types of Cu_2O electrodes was based on the previous research.[31] In details, the calculations were conducted using the following equation:

$$\text{EE} = \sum (1.23 + (-E_{\text{C}_{2+}})) * \text{FE}_{\text{C}_{2+}} / (1.23 + (-E))$$

where $E_{\text{C}_{2+}}$ is the thermodynamic potential (vs. RHE) of CO_2 electrochemical reduction to corresponding product; $\text{FE}_{\text{C}_{2+}}$ is the measured Faradaic efficiency in percentage for individual product; E is the applied potential vs. RHE.

2.3.5. CO stripping

The electrochemical CO stripping experiment was conducted in 1 M KOH electrolyte with the catalyst-coated glassy carbon electrode. For details, the electrolyte was first bubbled with pure Ar (99.999%) for 20 min to drive out other gases. Then Ar was switched to pure CO (99.999%) for another 20 min while the potential of the electrode was held constant at ~ 0 V (vs. RHE) to allow complete adsorption of CO onto the catalyst. At last, Ar was again purged into the electrolyte for 20 mins to remove excess CO followed by a CV sweep setup at 20 mV/s.

2.3.6. In-situ Raman spectra

In situ Raman spectra were recorded with a Renishaw InVia Reflex Raman spectrometer using a 633 nm excitation laser (17 mW). The photons were dispersed by a 1800 l/mm grating and collected by a spectrometer. Each Raman spectrum was collected by one acquisition for 20 s. To exhibit the real reaction condition of Cu_2O electrodes we used the in-situ Raman flow cell that can operate at relatively high current densities. Spectra were collected under different constant current density range from -50 mA cm^{-2} to -250 mA cm^{-2} . The electrolysis was held for 300 s for each current density and the signal was collected within the last 30 s. For the long-term surface status monitoring, a new electrode was employed and the current density was kept at 50 mA cm^{-2} with a sampling interval of 3 min. During test, CO_2 gas was continuously purged into gas chamber behind the backside of GDE so that ample gas reactant supply could be ensured. The cathode and anode electrolyte were both 1 M KOH flowed via peristaltic pumps, and two chambers were separated by a piece of AEM.

2.4. DFT calculation

Density functional theory (DFT) calculations were performed by using the Vienna ab initio simulation package (VASP), using the planewave basis with an energy cutoff of 500 eV, the projector augmented wave (PAW) potentials. The generalized gradient approximation with the function of Perdew–Burke–Ernzerhof (GGA-PBE) was applied to describe the exchange–correlation function. Grimme's semiempirical DFT-D3 scheme of dispersion correction was adopted to describe the van der Waals (vdW) interactions. The convergence criteria of the residual Hellmann–Feynman force and energy during structure optimization were set to 0.02 eV \AA^{-1} and 10^{-5} eV, respectively. Cu (111) surface and the $\text{Cu}_2\text{O}(111)/\text{Cu}(111)$ was modeled with 20 \AA vacuum to ensure no

interaction between two adjacent slabs. The Brillouin zone was sampled using $2 \times 2 \times 1$ k-mesh for the calculation.

The change of Gibbs free energy for each step was calculated as the following equation:

$$\Delta G = \Delta E + \Delta ZPE - T\Delta S + \Delta G_U + \Delta G_{\text{pH}} + \Delta G_{\text{field}}$$

where ΔE , ΔZPE and ΔS are the difference in DFT-calculated total energy difference between the reactant and the product, contributions of the zero-point energy to the free-energy change and the change in entropy between the products and reactants, respectively. T is the temperature and taken as 298.15 K. $\Delta G_U = -eU$, where U is the electrode potential with respect to the standard hydrogen electrode and e is the transferred charge. ΔG_{pH} is the correction H^+ free energy by the concentration, which can be calculated through $\Delta G_{\text{pH}} = k_B T \times \ln 10 \times \text{pH}$, where k_B is the Boltzmann constant and pH = 0 is assumed in the acidic medium in this calculation. ΔG_{field} is the free-energy correction resulting from the electrochemical double layer, which is neglected in the present study.

3. Results and discussions

3.1. Characterization of Cu_2O with different nanostructures

We first characterized the two types of Cu_2O nanomaterial with various technologies. The SEM images show that both types of Cu_2O were uniform nanospheres with a diameter of ~ 190 nm (Figs. S1 and S2). The different texture of the two samples can be further observed in the TEM images. $\text{Cu}_2\text{O}-1$ nanosphere exhibits a solid texture (Fig. 1A), and the corresponding selected area electron diffraction (SAED) pattern consisted of discontinuous bright diffraction spots and weak diffraction rings (Fig. 1B). The high-resolution TEM (HRTEM) image reveals the continuous lattice fringes over a relatively large area in the particle (Fig. S3). In contrast, $\text{Cu}_2\text{O}-2$ nanosphere is highly porous and contains visible voids within the particle (Fig. 1C). The corresponding SAED pattern exhibits continuous strong diffraction rings, which indicated its polycrystalline nature with random grains orientation (Fig. 1D). Further observation showed that each $\text{Cu}_2\text{O}-2$ nanosphere consists of interconnected small nanocrystallites with lattice fringes belonging to different faces (Fig. S4). The XRD patterns further confirmed the pure Cu_2O phase of both samples (Fig. 1E). Grain sizes of the Cu_2O nanospheres were calculated to be 22.2 and 7.8 nm for $\text{Cu}_2\text{O}-1$ and $\text{Cu}_2\text{O}-2$, based on the strongest Cu_2O (111) diffraction peak using the Scherrer equation. Compared with $\text{Cu}_2\text{O}-1$, the porous texture and polycrystalline nature of $\text{Cu}_2\text{O}-2$ result in enlarged specific surface area as revealed by the N_2 sorption isotherm (Fig. S5).

The above characterizations indicated that the two types of Cu_2O nanospheres exhibited distinct microstructures. $\text{Cu}_2\text{O}-1$ was consisted of relatively large nanocrystallites with preferred orientation while $\text{Cu}_2\text{O}-2$ was composed of smaller randomly oriented nanocrystallites. The smaller grain size endowed the latter with abundant grain boundaries that can alter the electron transfer behavior [32,33] which might further tune the oxidation states during the electro-reduction process. To verify this hypothesis, the electronic conductivities of two Cu_2O samples were tested via a simple voltammetry method (Fig. 1F). The much smaller current response of $\text{Cu}_2\text{O}-2$ compared with that of $\text{Cu}_2\text{O}-1$ indicated a lower electronic conductivity. The conductivity discrepancy can also be reflected by the different band gaps of the two Cu_2O samples [34], where $\text{Cu}_2\text{O}-1$ showed a slightly larger band gap (Fig. S6).

3.2. Electrochemical CO_2 reduction performances

The CO_2 RR performance of the Cu_2O catalysts was evaluated in a flow cell setup under chronopotentiometry mode. The overall Faradaic efficiencies (FEs) of different C_{2+} products at various current densities were shown in Fig. 2A, which are mainly ethylene and ethanol as well as

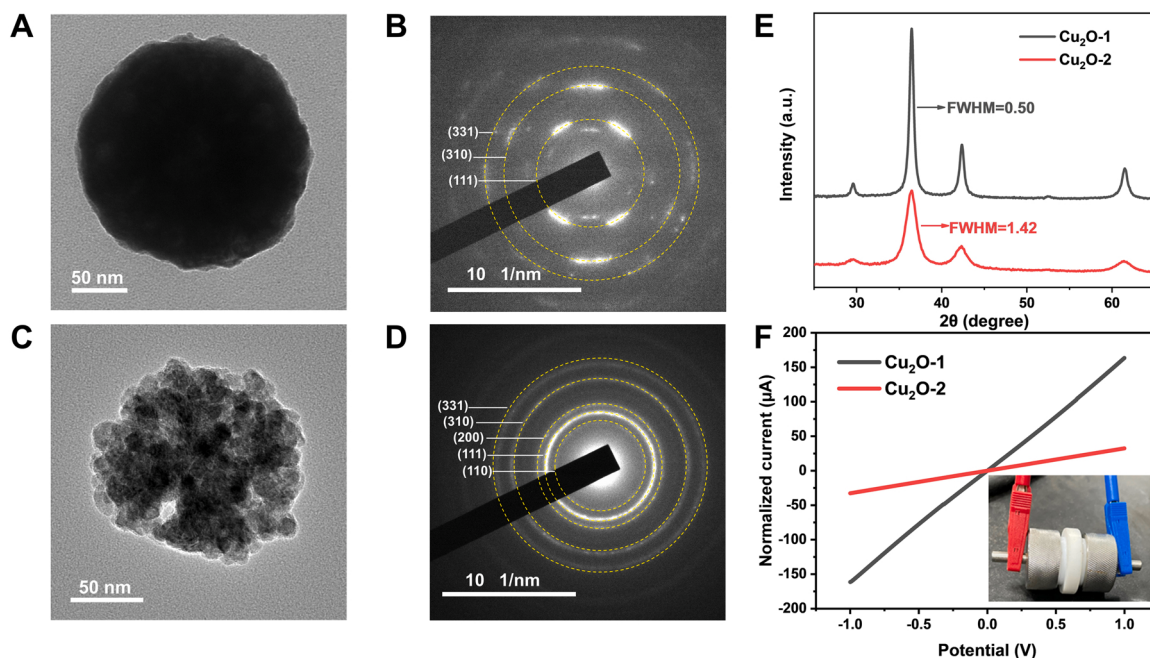


Fig. 1. Characterizations of the Cu_2O electrocatalysts. (A, C) TEM images and (B, D) SAED patterns of (A, B) Cu_2O -1; (C, D) Cu_2O -2. (E) XRD pattern showing the grain sizes difference and (F) Measurement of the electronic conductivity (insert showing the measuring setup).

a small amount of acetate and n-propanol (Figs. S7, S8). The Cu_2O -1 exhibited the highest C_{2+} FE of ~73% at a relatively low current density of 200 mA cm^{-2} . At higher current densities the FEs of C_{2+} products sharply decreased, while the FEs towards H_2 and CH_4 increased (Fig. S7). For Cu_2O -2, the FEs for C_{2+} products were low at low current densities and CO was the dominant CO_2 reduction product (Fig. S8). The FE towards C_{2+} products increased with increasing current densities and reached the maximum of ~79% at 800 mA cm^{-2} with C_2H_4 as the main product. Negligible CH_4 was observed only at current density over 900 mA cm^{-2} (Fig. S9). When referring to the C_{2+} partial current density, Cu_2O -2 showed a maximum of $692 \pm 34 \text{ mA cm}^{-2}$ while only $330 \pm 64 \text{ mA cm}^{-2}$ was achieved for Cu_2O -1 (Fig. 2B). Since the two electrodes exhibited comparable electrochemical active surface areas (ECSAs) (Fig. S10), the higher C_{2+} partial current density of Cu_2O -2 suggested the presence of highly active sites for multi-carbon products. The reaction kinetics toward C_2H_4 (the main C_{2+} product) was further compared via Tafel analysis. The Tafel slopes were 90 and 141 mV dec^{-1} for Cu_2O -2 and Cu_2O -1, respectively (Fig. 2C). The smaller Tafel slope indicated better reaction kinetics, which could be ascribed to the presence of highly active and efficient catalytic sites for C_2H_4 [35].

Cu_2O catalysts would be subjected to electroreduction during CO_2RR , leading to oxide-derived Cu as the true electrocatalysts. The in-situ electroreduction of Cu_2O catalysts was evaluated by cyclic voltammetry (CV) on a glassy carbon electrode. Both electrodes showed obvious reduction peaks within a potential range of -0.3 to -0.45 V vs. RHE, attributing to the reduction of Cu_xO to Cu (Fig. 2D). The two oxidation peaks can be ascribed to the oxidation of Cu to Cu^+ and Cu/Cu^+ to Cu^{2+} , respectively. Compared with Cu_2O -2, the Cu_2O -1 electrode exhibited more positive reduction potential and larger current density, indicating more pronounced reduction under negative potential and can be explained by its higher electronic conductivity as discussed earlier. This result suggested that the different microstructures of the two types of Cu_2O might affect the oxidation state of Cu during electrolysis. Since the catalytic performance of Cu-based catalysts is highly related to the oxidation state, we speculate that the distinct catalytic performance was attributed to the different electroreduction behavior of Cu_2O catalysts, which will be further discussed shortly.

Finally, the half-cell energy efficiency (EE) of two types of Cu_2O

electrodes were further compared (Fig. S11). Under high current density, the EE of Cu_2O -2 electrode was twice higher than that of Cu_2O -1. For the stability of the catalyst, Cu_2O -2 electrode maintained a high FE towards C_{2+} products of over 73% within a long period, among which the FE of C_2H_4 was about 45% (Fig. 2E). The FE of CO gradually decreased and CH_4 began to appear after 90 min electrolysis, indicating the dynamic composition (Cu^+ & Cu^0) changes of the catalyst during reaction. In contrast, for Cu_2O -1 electrode, the FE towards C_{2+} products sharply decreased within a short period of time (Fig. S12). In term of electrocatalytic CO_2 conversion towards C_{2+} products, the performance of Cu_2O -2 is among the best reports in literature (Table S2).

3.3. Characterizations of the electrodes during and after CO_2RR

To investigate the oxidation states and track the change of electrocatalysts during the CO_2RR process, the electrodes were further characterized after the galvanostatic electrolysis at -800 mA cm^{-2} . The solid spherical morphology of Cu_2O -1 was generally preserved while the surface became rough (Fig. S13). As depicted in the HRTEM image, the Cu_2O -1 AECR only showed continuous lattice fringes belonging to Cu (111), indicating the complete reduction to metallic Cu (Fig. 3A). This could be further verified by the SAED pattern that only shown the diffraction rings belonging to Cu (Fig. 3B). For Cu_2O -2 AECR, the assembled nanospheres were partially collapsed (Fig. S14), and exhibited lattice fringes belonging to both Cu (111) and Cu_2O (111) (Fig. 3C). The mixture state of Cu^0 and Cu^+ AECR was further confirmed by the SAED pattern (Fig. 3D). Despite the slight reconstruction of the electrocatalysts during electrolysis, the main micro-architectures were maintained. The different crystallographic compositions of the two types of Cu_2O electrodes AECR were also confirmed by the XRD patterns, where metallic Cu and mixed $\text{Cu}/\text{Cu}_2\text{O}$ phases were identified for Cu_2O -1 and Cu_2O -2, respectively (Fig. S15).

The surface status of the electrodes before and after CO_2RR was characterized by XPS. The Cu LMM Auger spectra indicated pure Cu^+ states of both electrodes before CO_2RR (Fig. S16). After CO_2 electrolysis, the relative ratios of Cu^+/Cu^0 were different for the two electrodes with the value 3.09 for Cu_2O -1 and 4.40 for Cu_2O -2 (Table S1 and Fig. S17). Despite the inevitable surface oxidation during sample transfer,³⁴ the

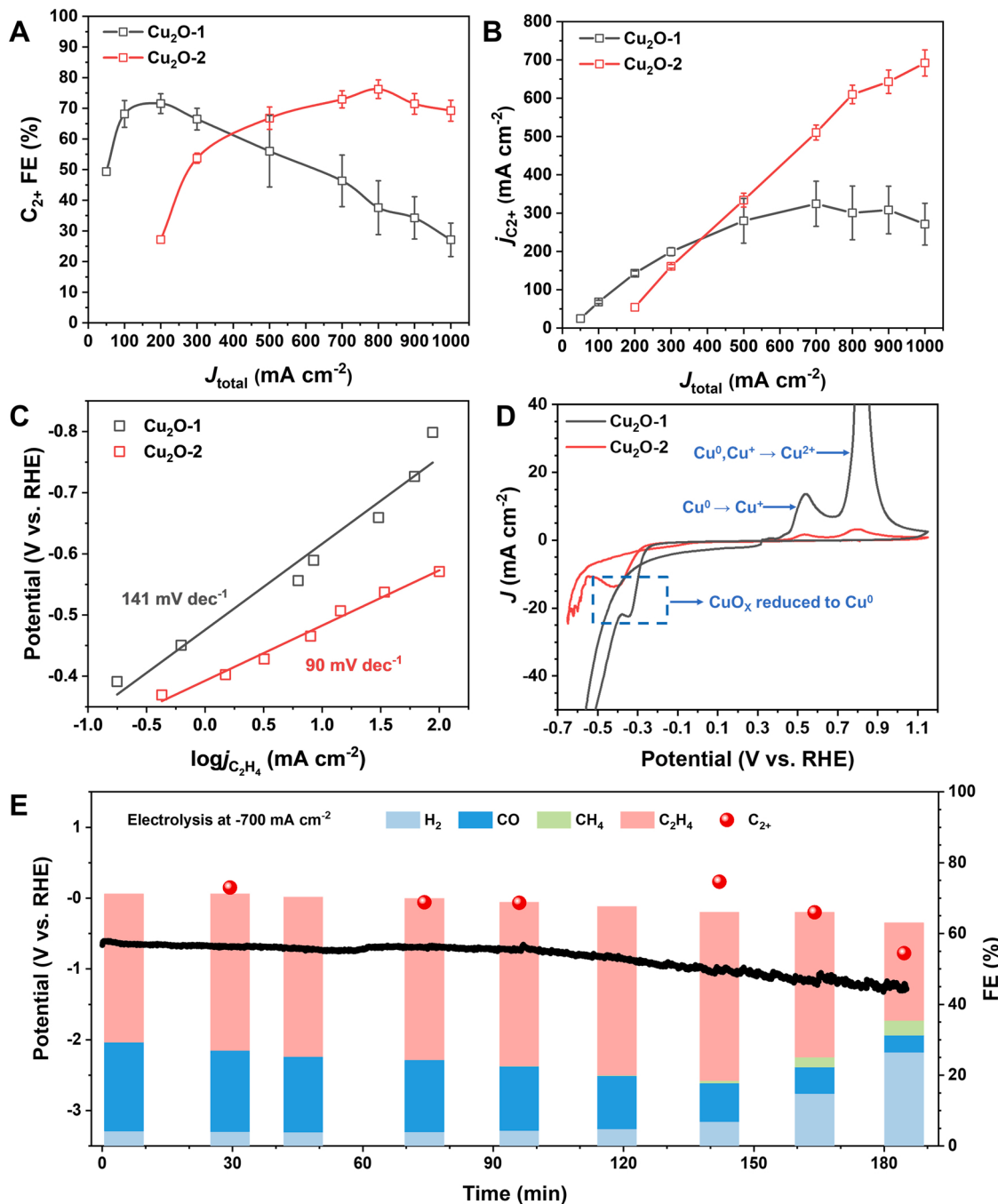


Fig. 2. Electrochemical CO_2 reduction performances of the Cu_2O electrocatalysts. (A) FE of the overall C_{2+} products and (B) partial current densities of two electrodes under different current densities. (C) Partial C_2H_4 current densities and Tafel slope of the two types electrodes. (D) Cyclic voltammetry (CV) curves of the two types of Cu_2O . (E) Stability test of $\text{Cu}_2\text{O}-2$ electrode under constant current electrolysis.

much higher Cu^+ content in the $\text{Cu}_2\text{O}-2$ AECR indicated the better preservation of Cu^+ species during CO_2RR .

In-situ Raman spectroscopic analysis was performed to monitor the surface species during CO_2RR . For $\text{Cu}_2\text{O}-1$ electrode, the Cu^+ band was only observed under open circuit potential (OCP) and after CV activation, which gradually vanished as current density increased (left panel in Fig. 3E). Interestingly, accompanied by the diminish of Cu^+ peak, the peaks assigned to $\text{CuO}_x/\text{(OH)}_y$ (co-adsorption of OH and oxygen on metallic Cu) [29] and Cu-O_{ad} [36] raised. This might be attributed to the rapid reduction of Cu_2O to Cu that led to more adsorbed oxygenate species. For $\text{Cu}_2\text{O}-2$, the Raman peak belongs to Cu_2O was retained under current densities ranging from 50 to 250 mA cm^{-2} (right panel in

Fig. 3E). Besides, a broad peak at $\sim 350 \text{ cm}^{-1}$ also appeared, which could be ascribed to the $\text{Cu}-\text{CO}$ stretch vibration [37,38]. Relatively weak band centered at $\sim 700 \text{ cm}^{-1}$ was assigned to surface hydroxyl species on Cu (Cu-OH_{ad}) [29]. For both electrodes, all the peaks decreased under high current densities, possibly due to the enhanced adsorption of $^*\text{H}$ and rapid generation of gas that interfered the Raman signals. Time-dependent in-situ Raman spectra were further conducted to study the dynamic change of the surface/subsurface Cu species with time. For $\text{Cu}_2\text{O}-1$ electrode, the Cu^+ peak intensity has decreased sharply within 1 min and completely vanished within 4 mins (left panel in Fig. 3F), which indicated a fast reduction process of Cu_2O . In contrast, for $\text{Cu}_2\text{O}-2$ electrode, the Cu^+ signal persisted after 50 mins with peak

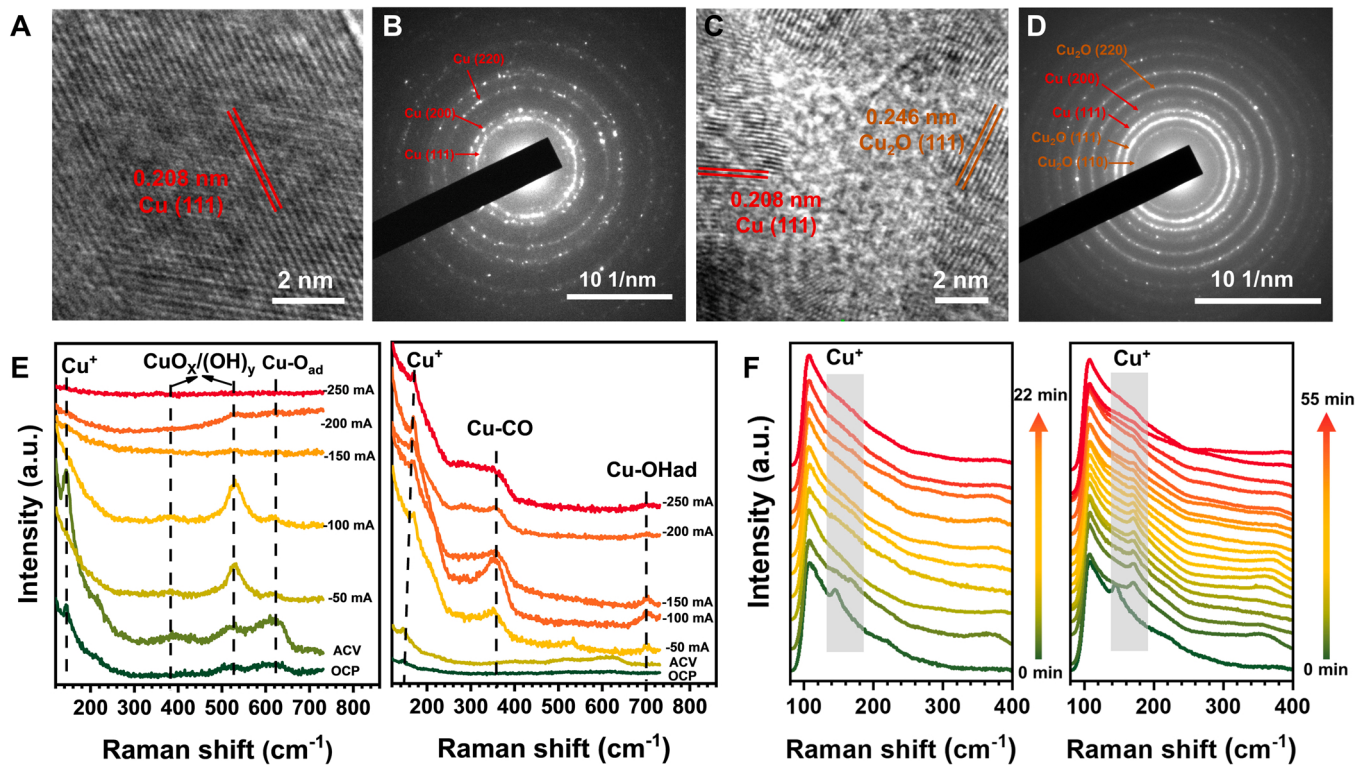


Fig. 3. Characterizations of the Cu₂O electrodes during and after CO₂RR. HRTEM images showing the composition and structures of the electrodes (A, B) Cu₂O-1 and (C, D) Cu₂O-2. (E) In-situ Raman spectra monitoring the surface of the two electrodes under different current densities. Left for Cu₂O-1 electrode and right for Cu₂O-2 electrode. (F) Time dependent in-situ Raman spectra monitoring the dynamic changes on surface/subsurface. Left for Cu₂O-1 electrode and right for Cu₂O-2 electrode.

intensity gradually decreased with prolonged reaction time (right panel in Fig. 3F), which indicated its much more sluggish reduction kinetics. Obviously, the Cu₂O-2 electrode would better preserve the Cu⁺ species on the catalyst surface during electrolysis, thus maintaining mixed Cu⁺/Cu⁰ states.

3.4. Mechanism exploration

To verify that the dynamic change of Cu₂O nanospheres (electro-reduction of Cu⁺ to Cu⁰) was governed by the electronic conductivity of the electrocatalysts, control experiments were performed by incorporating carbon nanotubes (CNTs) into the Cu₂O-2 electrode. The highly conductive CNTs would modulate the electronic conductivity and thus affecting the redox behavior, as proved by the notably positive shifted reduction peak of Cu₂O and more pronounced reversed oxidation peaks with a small amount of CNTs (Cu₂O-2/C = 4, mass ratio) (Fig. 4A). Increasing the amount of CNTs leads to a further decreased total FE of C₂₊ products at a fixed current density of 800 mA cm⁻² (Figs. 4B, S18 and S19). Furthermore, pure CNTs electrode was inactive for CO₂RR and mainly produced H₂ (Fig. S20). Other conductive carbons such as carbon black (CB) showed a similar effect on modulating the product selectivity (Fig. S21), again verifying that the dynamic evolution of electrocatalyst strongly depends on the conductivity [39]. If Cu₂O-2 was pre-electrochemically reduced to oxide-derived Cu (ODCu), the C₂₊ FE was even lower (Fig. S22). The catalytic performance could be largely recovered when the ODCu electrode was re-oxidized. Similar to Cu₂O-1 electrode, both Cu₂O-2/CNTs and ODCu electrodes exhibited enhanced formation of H₂ and CH₄ (Fig. S23), which is in line with the low Cu⁺/Cu ratio during electrolysis (Fig. S24). While the ECSAs of the ODCu electrode was almost the same with that of Cu₂O-2 electrode (Fig. S25), the different performance should be attributed to the different catalytic sites associating with the oxidation states. The different catalytic activity of Cu₂O catalysts towards C₂₊ product is consistent with their Tafel slopes

of the corresponding partial current density. The Tafel slopes of the C₂H₄ partial current densities were 111 and 138 mV dec⁻¹ for Cu₂O-2/CNTs and ODCu, which were notably higher than that of Cu₂O-2 (90 mV dec⁻¹) (Fig. S26).

Based on the above discussion, we can conclude that the product selectivity of Cu₂O electrocatalysts is highly related to the valence state of surface Cu sites, while the dynamic transformation of Cu⁺ to Cu⁰ during electrolysis would be affected by the microstructure of the catalysts. According to previous reports, Cu⁺ dominated surface governs CO₂RR towards CO/HCOOH [24,40], and Cu⁰ dominated surface tends to produce H₂ and CH₄ [41,42]; only the coexistence of Cu⁺ and Cu⁰ sites favors the formation of C₂₊ products [11,19,20]. Thus, the dynamic evolution of Cu₂O catalysts during electrolysis would explain the distinct electrocatalytic performance of the two electrodes. Specifically, at low current densities (equal to low overpotential) Cu₂O-1 would be easily reduced to a mixture of Cu⁰/Cu⁺ and achieve a high FE for C₂₊; meanwhile, the Cu₂O-2 would mostly preserve the Cu⁺ species due to its resistance to electroreduction and favor the formation of CO. Further increasing the current density/overpotential leads to the complete reduction of Cu₂O-1 to Cu⁰ but a mixed Cu⁰/Cu⁺ state for Cu₂O-2, in line with the increased formation of CH₄ for Cu₂O-1 and promoted C₂₊ formation for Cu₂O-2.

Since CO is a key reaction intermediate for CO₂RR, the binding strength between CO intermediate and electrocatalysts was investigated by CO temperature-programmed desorption (CO-TPD) (Fig. 4C). The Cu₂O-1 exhibited two CO desorption peaks at 471.6 K (peak 1) and 598.7 K (peak 2) while the two peaks for Cu₂O-2 were at 475.7 K and 605.6 K, respectively. The main desorption peak (peak 2) of Cu₂O-2 at a higher desorption temperature indicated stronger binding with CO [43]. Enhanced CO adsorption has been reported on defects or low coordinated sites [44,45], and the abundant grain boundaries within the Cu₂O-2 should be accounted for the enhanced CO binding, which can suppress HER and boost CO₂RR process [44,46,47]. The quasi

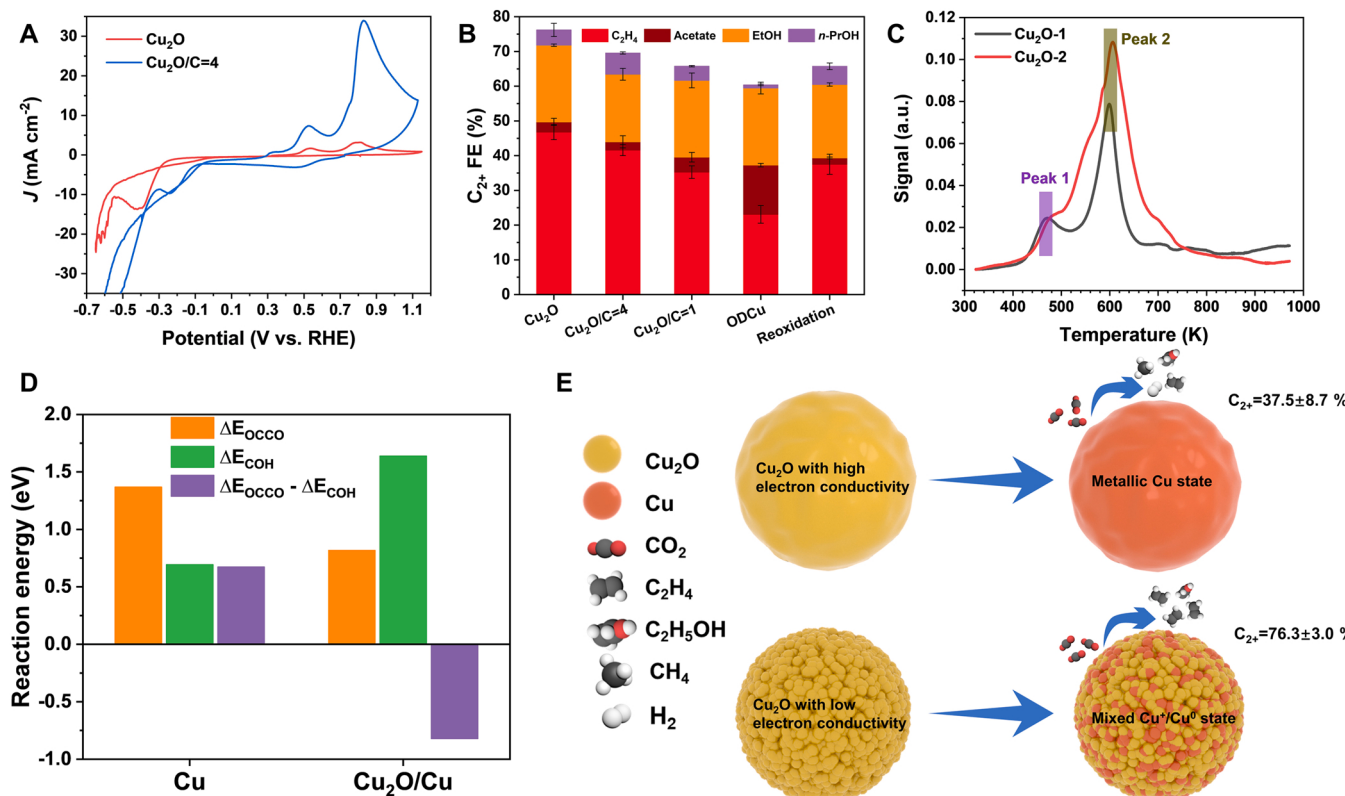


Fig. 4. Mechanism exploration of the Cu_2O electrocatalysts. (A) Comparison of the redox behavior between $\text{Cu}_2\text{O}-2$ and $\text{Cu}_2\text{O}-2/\text{CNTs}$. (B) FE of the overall C_{2+} products of $\text{Cu}_2\text{O}-2$ -based electrodes with different compositions under 800 mA cm^{-2} . (C) CO-TPD of Cu_2O electrocatalysts. (D) DFT calculations showing the free energy related to the pathways of $^{*}\text{CO}$ dimerization and $^{*}\text{CO}$ hydrogenation on different surface. (E) Schematic diagram showing different micro-architectures tuning the oxidation state of Cu_2O electrocatalysts that eventually resulting in different catalytical performances.

adsorption quantity corresponding to each peak was shown in Fig. S27. The adsorption quantity (peak 2) of $\text{Cu}_2\text{O}-2$ was almost three times higher than that of $\text{Cu}_2\text{O}-1$. The enhanced CO adsorption on $\text{Cu}_2\text{O}-2$ further supported by electrochemical CO-striping measurements (Fig. S28).

Density function theory (DFT) calculations were further conducted to explain the product selectivity of CO_2RR on Cu-based catalysts with different valence states. Dimerization and hydrogenation of $^{*}\text{CO}$ have been regarded as the rate-determining step (RDS) toward C_{2+} products and CH_4 , respectively [48–51]. Therefore, the reaction pathways of $^{*}\text{CO}$ dimerization and $^{*}\text{CO}$ hydrogenation at Cu surface with different oxidation states were calculated (Figs. 4D and S29). At completely reduced Cu_2O (Cu metal), $^{*}\text{CO}$ hydrogenation to $^{*}\text{COH}$ was favored over $^{*}\text{CO}$ dimerization. In contrast, for partly reduced Cu_2O (denoted as $\text{Cu}_2\text{O}/\text{Cu}$) with mixture valence states of Cu^+/Cu^0 , dimerization of $^{*}\text{CO}$ was much favored. For the $^{*}\text{CO}$ dimerization process, the Gibbs free energy (ΔG) at partly reduced Cu_2O was 0.82 eV , which was much lower than that on metallic Cu surface ($\Delta G = 1.37 \text{ eV}$). These results indicated that coexistence of Cu^+ and Cu^0 can greatly lower the energy barrier for the C-C coupling process thus favoring C_{2+} products, which is consistent with the experimental results. From the discussion above, we can conclude that the distinct catalytic performance between two types of Cu_2O can be attributed to the oxidation states and composition variation during CO_2RR . Through grain boundary refining, the electron transfer process can be modulated, which affects the true valence state and catalytic sites of electrocatalysts at operational conditions as schematically depicted in Fig. 4E.

4. Conclusions

In summary, we report a grain refining approach to regulate the

valence states of Cu-based electrocatalysts during CO_2RR . $\text{Cu}_2\text{O}-2$ nanospheres with abundant grain boundaries exhibit a maximum FE of $\sim 79\%$ for C_{2+} products and a highest $j_{\text{C}2+}$ of $692 \pm 34 \text{ mA cm}^{-2}$, much superior to the $\text{Cu}_2\text{O}-1$ with a solid texture. Such different catalytic performance has been mainly attributed to the distinct valence state of catalysts during electrolysis. Due to the retarded electron transfer by the grain boundaries, Cu^+ species could be better preserved in $\text{Cu}_2\text{O}-2$ at high current densities during CO_2RR process as revealed by both in-situ and ex-situ characterizations. Besides, CO as a key intermediate would be better stabilized on the grain-boundary-rich $\text{Cu}_2\text{O}-2$ catalyst. DFT calculations confirmed that the coexistence of Cu^+/Cu^0 species leads to decreased energy barrier for CO dimerization, thus promoting the formation of C_{2+} products. The present work demonstrates an efficient strategy to regulate the valence state of the real catalytic active sites under operational conditions.

CRediT authorship contribution statement

Xiangzhou Lv: Conceptualization, Methodology, Investigation, Formal analysis, Writing – original draft. **Qian Liu:** Investigation, Formal analysis. **Jianghao Wang:** Investigation, Formal analysis. **Xiaojun Wu:** Investigation, Validation. **Xiaotong Li:** Formal analysis. **Yue Yang:** Formal analysis. **Jianhua Yan:** Writing – review & editing. **Angjian Wu:** Methodology, Resources, Writing – review & editing. **Hao Bin Wu:** Conceptualization, Methodology, Funding acquisition, Writing – review & editing, Supervision, Project administration.

Declaration of Competing Interest

The authors declare that they have no known competing financial interests or personal relationships that could have appeared to influence

the work reported in this paper.

Data availability

Data will be made available on request.

Acknowledgments

H.B.W. acknowledges the funding support from Natural Science Foundation of Zhejiang Province (Grant No. LR21E020003), National Natural Science Foundation of China (Grant No. 22005266), and “the Fundamental Research Funds for the Central Universities” (2021FZXX001-09). A. Wu acknowledges the support from the Pioneer R&D Program of Zhejiang Province (2022C03040), the “the Fundamental Research Funds for the Central Universities” (226-2022-00091), and the Baima Lake Laboratory. We thank Chao Bi from the core facility platform of Zhejiang University School of Medicine for in-situ Raman characterization. We also thank Shiyanjia Lab (www.shiyanjia.com) for the XPS, BET and NMR test.

Appendix A. Supplementary material

Supplementary data associated with this article can be found in the online version at [doi:10.1016/j.apcatb.2022.122272](https://doi.org/10.1016/j.apcatb.2022.122272).

References

- [1] P. De Luna, C. Hahn, D. Higgins, S.A. Jaffer, T.F. Jaramillo, E.H. Sargent, What would it take for renewably powered electrosynthesis to displace petrochemical processes? *Science* 364 (2019) eaav3506.
- [2] M.T. Tang, H. Peng, P.S. Lamoureux, M. Bajdich, F. Abild-Pedersen, From electricity to fuels: descriptors for C1 selectivity in electrochemical CO₂ reduction, *Appl. Catal. B Environ.* 279 (2020), 119384.
- [3] R. Pang, P. Tian, H. Jiang, M. Zhu, X. Su, Y. Wang, X. Yang, Y. Zhu, L. Song, C. Li, Tracking structural evolution: operando regenerative CeO_x/Bi interface structure for high-performance CO₂ electroreduction, *Natl. Sci. Rev.* 8 (2020).
- [4] W. Ma, X. He, W. Wang, S. Xie, Q. Zhang, Y. Wang, Electrocatalytic reduction of CO₂ and CO to multi-carbon compounds over Cu-based catalysts, *Chem. Soc. Rev.* 50 (2021) 12897–12914.
- [5] H. Li, S. Cao, H. Sun, Y. Lu, Y. Zhang, X. Lu, J. Zeng, Z. Yan, CuNCN derived Cu-based/CxNy catalysts for highly selective CO₂ electroreduction to hydrocarbons, *Appl. Catal. B Environ.* 320 (2023), 121948.
- [6] W. Dan, J. Gui, B. Pan, M. Li, Y. Kuang, C. Zhang, J. Mao, Y. Loua, C. Pan, F. Li, Y. Li, Y. Wang, Y. Zhu, Y. Zhang, Multi-microenvironment synergistically promoting CO₂ electroreduction activity on porous Cu nanosheets, *Appl. Catal. B Environ.* (2022), 122119.
- [7] W. Ma, S. Xie, T. Liu, Q. Fan, J. Ye, F. Sun, Z. Jiang, Q. Zhang, J. Cheng, Y. Wang, Electrocatalytic reduction of CO₂ to ethylene and ethanol through hydrogen-assisted C–C coupling over fluorine-modified copper, *Nat. Catal.* 3 (2020) 478–487.
- [8] D. Gao, I. Zegkinoglou, N.J. Divins, F. Scholten, I. Sinev, P. Grosse, B. Roldan Cuena, Plasma-activated copper nanocube catalysts for efficient carbon dioxide electroreduction to hydrocarbons and alcohols, *ACS Nano* 11 (2017) 4825–4831.
- [9] G. Iijima, H. Yamaguchi, T. Inomata, H. Yoto, M. Ito, H. Masuda, Methanethiol SAMs induce reconstruction and formation of Cu⁺ on a Cu catalyst under electrochemical CO₂ reduction, *ACS Catal.* 10 (2020) 15238–15249.
- [10] T.-C. Chou, C.-C. Chang, H.-L. Yu, W.-Y. Yu, C.-L. Dong, J.-J. Velasco-Vélez, C.-H. Chuang, L.-C. Chen, J.-F. Lee, J.-M. Chen, H.-L. Wu, Controlling the oxidation state of the Cu electrode and reaction intermediates for electrochemical CO₂ reduction to ethylene, *J. Am. Chem. Soc.* 142 (2020) 2857–2867.
- [11] H. Mistry, A.S. Varela, C.S. Bonifacio, I. Zegkinoglou, I. Sinev, Y.-W. Choi, K. Kisslinger, E.A. Stach, J.C. Yang, P. Strasser, B.R. Cuena, Highly selective plasma-activated copper catalysts for carbon dioxide reduction to ethylene, *Nat. Commun.* 7 (2016) 12123.
- [12] Y. Zhou, F. Che, M. Liu, C. Zou, Z. Liang, P. De Luna, H. Yuan, J. Li, Z. Wang, H. Xie, H. Li, P. Chen, E. Bladt, R. Quintero-Bermudez, T.-K. Sham, S. Bals, J. Hofkens, D. Sinton, G. Chen, E.H. Sargent, Dopant-induced electron localization drives CO₂ reduction to C₂ hydrocarbons, *Nat. Chem.* 10 (2018) 974–980.
- [13] W. Ni, C. Li, X. Zang, M. Xu, S. Huo, M. Liu, Z. Yang, Y.-M. Yan, Efficient electrocatalytic reduction of CO₂ on Cu₂O decorated graphene oxides: an insight into the role of multivalent Cu in selectivity and durability, *Appl. Catal. B Environ.* 259 (2019), 118044.
- [14] C.W. Li, M.W. Kanan, CO₂ reduction at low overpotential on Cu electrodes resulting from the reduction of thick Cu₂O films, *J. Am. Chem. Soc.* 134 (2012) 7231–7234.
- [15] D. Ren, Y. Deng, A.D. Handoko, C.S. Chen, S. Malkhandi, B.S. Yeo, Selective electrochemical reduction of carbon dioxide to ethylene and ethanol on copper(I) oxide catalysts, *ACS Catal.* 5 (2015) 2814–2821.
- [16] A.D. Handoko, K.W. Chan, B.S. Yeo, –CH₃ mediated pathway for the electroreduction of CO₂ to ethane and ethanol on thick oxide-derived copper catalysts at low overpotentials, *ACS Energy Lett.* 2 (2017) 2103–2109.
- [17] S. Mu, H. Lu, Q. Wu, L. Li, R. Zhao, C. Long, C. Cui, Hydroxyl radicals dominate reoxidation of oxide-derived Cu in electrochemical CO₂ reduction, *Nat. Commun.* 13 (2022) 3694.
- [18] Z.-Q. Liang, T.-T. Zhuang, A. Seifitokaldani, J. Li, C.-W. Huang, C.-S. Tan, Y. Li, P. De Luna, C.T. Dinh, Y. Hu, Q. Xiao, P.-L. Hsieh, Y. Wang, F. Li, R. Quintero-Bermudez, Y. Zhou, P. Chen, Y. Pang, S.-C. Lo, L.-J. Chen, H. Tan, Z. Xu, S. Zhao, D. Sinton, E.H. Sargent, Copper-on-nitride enhances the stable electrosynthesis of multi-carbon products from CO₂, *Nat. Commun.* 9 (2018) 3828.
- [19] X. Yuan, S. Chen, D. Cheng, L. Li, W. Zhu, D. Zhong, Z.-J. Zhao, J. Li, T. Wang, J. Gong, Controllable Cu⁰–Cu⁺ sites for electrocatalytic reduction of carbon dioxide, *Angew. Chem. Int. Ed.* 60 (2021) 15344–15347.
- [20] H. Xiao, W.A. Goddard, T. Cheng, Y. Liu, Cu metal embedded in oxidized matrix catalyst to promote CO₂ activation and CO dimerization for electrochemical reduction of CO₂, *Proc. Natl. Acad. Sci.* 114 (2017) 6685.
- [21] S. Lee, D. Kim, J. Lee, Electrocatalytic production of C₃–C₄ compounds by conversion of CO₂ on a chloride-induced bi-phasic Cu₂O–Cu catalyst, *Angew. Chem. Int. Ed.* 54 (2015) 14701–14705.
- [22] Y. Lum, J.W. Ager, Stability of residual oxides in oxide-derived copper catalysts for electrochemical CO₂ reduction investigated with ¹⁸O labeling, *Angew. Chem. Int. Ed.* 57 (2018) 551–554.
- [23] Z.-Z. Wu, F.-Y. Gao, M.-R. Gao, Regulating the oxidation state of nanomaterials for electrocatalytic CO₂ reduction, *Energy Environ. Sci.* 14 (2021) 1121–1139.
- [24] J. Wang, H.-Y. Tan, Y. Zhu, H. Chu, H.M. Chen, Linking the dynamic chemical state of catalysts with the product profile of electrocatalytic CO₂ reduction, *Angew. Chem. Int. Ed.* 60 (2021) 17254–17267.
- [25] C. Chen, X. Sun, L. Lu, D. Yang, J. Ma, Q. Zhu, Q. Qian, B. Han, Efficient electroreduction of CO₂ to C₂ products over B-doped oxide-derived copper, *Green Chem.* 20 (2018) 4579–4583.
- [26] T.T.H. Hoang, S. Verma, S. Ma, T.T. Fister, J. Timoshenko, A.I. Frenkel, P.J. A. Kenis, A.A. Gewirth, Nanoporous copper–silver alloys by additive-controlled electrodeposition for the selective electroreduction of CO₂ to ethylene and ethanol, *J. Am. Chem. Soc.* 140 (2018) 5791–5797.
- [27] R.M. Arán-Ais, F. Scholten, S. Kunze, R. Rizo, B. Roldan Cuena, The role of in situ generated morphological motifs and Cu(I) species in C₂₊ product selectivity during CO₂ pulsed electroreduction, *Nat. Energy* 5 (2020) 317–325.
- [28] R. Casebolt, K. Levine, J. Suntivich, T. Hanrath, Pulse check: potential opportunities in pulsed electrochemical CO₂ reduction, *Joule* 5 (2021) 1987–2026.
- [29] Y. Zhao, X. Chang, A.S. Malkani, X. Yang, L. Thompson, F. Jiao, B. Xu, Speciation of Cu surfaces during the electrochemical CO reduction reaction, *J. Am. Chem. Soc.* 142 (2020) 9735–9743.
- [30] P.-P. Yang, X.-L. Zhang, F.-Y. Gao, Y.-R. Zheng, Z.-Z. Niu, X. Yu, R. Liu, Z.-Z. Wu, S. Qin, L.-P. Chi, Y. Duan, T. Ma, X.-S. Zheng, J.-F. Zhu, H.-J. Wang, M.-R. Gao, S.-H. Yu, Protecting copper oxidation state via intermediate confinement for selective CO₂ electroreduction to C₂₊ fuels, *J. Am. Chem. Soc.* 142 (2020) 6400–6408.
- [31] M.G. Kibria, C.-T. Dinh, A. Seifitokaldani, P. De Luna, T. Burdyny, R. Quintero-Bermudez, M.B. Ross, O.S. Bushuyev, F.P. García de Arquer, P. Yang, D. Sinton, E. H. Sargent, A surface reconstruction route to high productivity and selectivity in CO₂ electroreduction toward C₂₊ hydrocarbons, *Adv. Mater.* 30 (2018) 1804867.
- [32] W. Tsien Adam, L. Brown, P. Levendorf Mark, F. Ghahari, Y. Huang Pinshane, W. Havener Robin, S. Ruiz-Vargas Carlos, A. Muller David, P. Kim, J. Park, Tailoring electrical transport across grain boundaries in polycrystalline graphene, *Science* 336 (2012) 1143–1146.
- [33] F. Greuter, G. Blatter, Electrical properties of grain boundaries in polycrystalline compound semiconductors, *Semicond. Sci. Technol.* 5 (1990) 111–137.
- [34] L. Zhang, L. McMillon, J. McNatt, Gas-dependent bandgap and electrical conductivity of Cu₂O thin films, *Sol. Energy Mater. Sol. Cells* 108 (2013) 230–234.
- [35] X. Li, Q. Liu, J. Wang, D. Meng, Y. Shu, X. Lv, B. Zhao, H. Yang, T. Cheng, Q. Gao, L. Li, H.B. Wu, Enhanced electroreduction of CO₂ to C₂₊ products on heterostructured Cu/oxide electrodes, *Chem* 8 (2022) 2148–2162.
- [36] F. Shao, J.K. Wong, Q.H. Low, M. Iannuzzi, J. Li, J. Lan, In situ spectroelectrochemical probing of CO redox landscape on copper single-crystal surfaces, *Proc. Natl. Acad. Sci.* 119 (2022) e2118166119.
- [37] V. Chernyshova Irina, P. Somasundaran, S. Ponmurangam, On the origin of the elusive first intermediate of CO₂ electroreduction, *Proc. Natl. Acad. Sci.* 115 (2018) E9261–E9270.
- [38] S. Jiang, K. Klingan, C. Pasquini, H. Dau, New aspects of operando Raman spectroscopy applied to electrochemical CO₂ reduction on Cu foams, *J. Chem. Phys.* 150 (2018), 041718.
- [39] L. Zhang, F. Mao, L.R. Zheng, H.F. Wang, X.H. Yang, H.G. Yang, Tuning metal catalyst with metal–C₃N₄ interaction for efficient CO₂ electroreduction, *ACS Catal.* 8 (2018) 11035–11041.
- [40] C.-J. Chang, S.-F. Hung, C.-S. Hsu, H.-C. Chen, S.-C. Lin, Y.-F. Liao, H.M. Chen, Quantitatively unraveling the redox shuttle of spontaneous oxidation/electroreduction of Cu₂O on silver nanowires using in situ X-ray absorption spectroscopy, *ACS Cent. Sci.* 5 (2019) 1998–2009.
- [41] Z. Weng, Y. Wu, M. Wang, J. Jiang, K. Yang, S. Huo, X.-F. Wang, Q. Ma, G. W. Brudvig, V.S. Batista, Y. Liang, Z. Feng, H. Wang, Active sites of copper-complex catalytic materials for electrochemical carbon dioxide reduction, *Nat. Commun.* 9 (2018) 415.
- [42] S.-C. Lin, C.-C. Chang, S.-Y. Chiu, H.-T. Pai, T.-Y. Liao, C.-S. Hsu, W.-H. Chiang, M.-K. Tsai, H.M. Chen, Operando time-resolved X-ray absorption spectroscopy reveals the chemical nature enabling highly selective CO₂ reduction, *Nat. Commun.* 11 (2020) 3525.

- [43] S. Vollmer, G. Witte, C. Wöll, Determination of site specific adsorption energies of CO on copper, *Catal. Lett.* 77 (2001) 97–101.
- [44] A. Verdaguier-Casadevall, C.W. Li, T.P. Johansson, S.B. Scott, J.T. McKeown, M. Kumar, I.E.L. Stephens, M.W. Kanan, I. Chorkendorff, Probing the active surface sites for CO reduction on oxide-derived copper electrocatalysts, *J. Am. Chem. Soc.* 137 (2015) 9808–9811.
- [45] F. Scholten, K.-L.C. Nguyen, J.P. Bruce, M. Heyde, B. Roldan Cuenya, Identifying structure-selectivity correlations in the electrochemical reduction of CO₂: a comparison of well-ordered atomically clean and chemically etched copper single-crystal surfaces, *Angew. Chem. Int. Ed.* 60 (2021) 19169–19175.
- [46] X. Feng, K. Jiang, S. Fan, M.W. Kanan, A direct grain-boundary-activity correlation for CO electroreduction on Cu nanoparticles, *ACS Cent. Sci.* 2 (2016) 169–174.
- [47] G. Mariano Ruperto, K. McKelvey, S. White Henry, W. Kanan Matthew, Selective increase in CO₂ electroreduction activity at grain-boundary surface terminations, *Science* 358 (2017) 1187–1192.
- [48] W. Li, L. Li, Q. Xia, S. Hong, L. Wang, Z. Yao, T.-S. Wu, Y.-L. Soo, H. Zhang, T.W. B. Lo, A.W. Robertson, Q. Liu, L. Hao, Z. Sun, Lowering C–C coupling barriers for efficient electrochemical CO₂ reduction to C₂H₄ by jointly engineering single Bi atoms and oxygen vacancies on CuO, *Appl. Catal. B Environ.* 318 (2022), 121823.
- [49] J.H. Montoya, C. Shi, K. Chan, J.K. Nørskov, Theoretical insights into a CO dimerization mechanism in CO₂ electroreduction, *J. Phys. Chem. Lett.* 6 (2015) 2032–2037.
- [50] X.Y. Zhang, W.J. Li, X.F. Wu, Y.W. Liu, J. Chen, M. Zhu, H.Y. Yuan, S. Dai, H. F. Wang, Z. Jiang, P.F. Liu, H.G. Yang, Selective methane electrosynthesis enabled by a hydrophobic carbon coated copper core–shell architecture, *Energy Environ. Sci.* 15 (2022) 234–243.
- [51] R. Kortlever, J. Shen, K.J.P. Schouten, F. Calle-Vallejo, M.T.M. Koper, Catalysts and reaction pathways for the electrochemical reduction of carbon dioxide, *J. Phys. Chem. Lett.* 6 (2015) 4073–4082.